Optics Communications 479 (2021) 126413

Contents lists available at ScienceDirect

Optics Communications

journal homepage: www.elsevier.com/locate/optcom

Black metal nanoparticles from abrasion processes in everyday life: Bicycle drivetrains and rock-climbing ropes

Hans Moosmüller [a,*], Ramesh Giri [b], Christopher M. Sorensen [b], Matthew J. Berg [b]

[a] LASSO—Laboratory for Aerosol Science, Spectroscopy, and Optics, DRI—Desert Research Institute, NSHE—Nevada System of Higher Education, 2215 Raggio Parkway, Reno, NV 89512, USA

[b] Department of Physics, Kansas State University, 1228 N. 17th Street, Manhattan, KS 66506-2601, USA

ARTICLE INFO

Keywords:
Metallic nanoparticles
Single scattering albedo
Appearance

ABSTRACT

Black objects are sometimes associated with black carbon, while shiny, highly reflecting surfaces are typically associated with metals. Here, we discuss several objects in everyday life that upon use take on a black color that is unlikely to be due to black carbon. We propose that this black color is caused by the formation of metallic nanoparticles from abrasion processes. We support this hypothesis using Mie theory and the fact that spherical metal particles are only shiny or bright if the imaginary part of their refractive index and its product with the particle size-parameter are both larger than three. While this is commonly true for bulk metals, the second condition is generally not fulfilled for metallic nanoparticles, and hence, such particles become highly absorbing, i.e., black. For the black grime accumulated on bicycle drivetrains and climbing ropes, we detected metal nanoparticles with electron microscopy, which likely originated from mechanical abrasion processes during use.

1. Introduction

In terms of visual appearance under white-light illumination, the whiteness of a particle is usually quantified by the single scattering albedo (SSA), which is the ratio of the scattering cross section C_{sca} and extinction cross section C_{ext} [1],

$$SSA = \frac{C_{sca}}{C_{ext}} = 1 - \frac{C_{abs}}{C_{ext}}. \quad (1)$$

In Eq. (1), C_{ext} is the sum of C_{sca} and the absorption cross section C_{abs} for a given wavelength λ of incident light. Due to the conservation of energy, the SSA is bounded as $0 < SSA \leq 1$. When the $SSA = 1$ across the visible wavelength range the appearance of a particle is described by terms like "white", "shiny", "bright", or "reflective", because all extinction is caused by scattering. If the SSA equals zero across the visible wavelength range, the term "black" is appropriate since the extinction is exclusively due to absorption. Values for the SSA between zero and one indicate an appearance in different shades of "gray", or possibly a colored appearance if the material exhibits a significant variation of its refractive index and SSA as function of wavelength. The term "white" used below will denote a particle exhibiting $0.7 < SSA \leq 1$, "gray" for $0.2 < SSA \leq 0.7$, and "black" for $SSA \leq 0.2$. Because of its connection to energy conservation, the SSA is also an important quantity in energy-budget considerations of physical systems involving light scattering from particles. For example, the SSA is the dominant intensive property for aerosol-particle radiative forcing in the atmosphere [2–4].

In the following, we consider two common objects encountered in everyday life, a bicycle drivetrain and a rock-climbing rope, where grime is produced through use that eventually takes on a black appearance. We propose that the black appearance originates from black metallic nanoparticles that accumulate in the grime due to mechanical abrasion and support this hypothesis with Mie theory and electron microscopy of the grime material. For simplicity, we focus our theoretical considerations on homogeneous spherical particles, hence the use of Mie theory [5].

The appearance, i.e., SSA here, of metallic nanoparticles is completely described in Mie theory by the particle's complex-valued refractive index $m = n + i\kappa$, where n and κ are the real and imaginary parts of m, respectively, and the size parameter $x = \pi D/\lambda$, where D is the particle diameter. Moreover, "Mie theory, limited though it may be, does provide a first-order description of optical effects in nonspherical particles, and it correctly describes many small-particle effects that are not intuitively obvious" [6]. While we use Mie theory to gain basic understanding of SSA, this approach is limited because the metallic particles considered here are not spherical and homogeneous as required by Mie theory and their number density is not sufficiently small for rigorous application of the single scattering concept [6]. We build upon existing discussions for the SSA in the small and large

* Corresponding author.
E-mail address: Hans.Moosmuller@dri.edu (H. Moosmüller).

https://doi.org/10.1016/j.optcom.2020.126413
Received 24 June 2020; Received in revised form 16 August 2020; Accepted 29 August 2020
Available online 1 September 2020
0030-4018/© 2020 The Authors. Published by Elsevier B.V. This is an open access article under the CC BY-NC-ND license (http://creativecommons.org/licenses/by-nc-nd/4.0/).

Fig. 1. Author's (HM) leg marked by black grime from the chainring. Also note the black appearance of the drive train.

Fig. 2. (a) Abraded climbing carabiner with red arrow indicating the location of the abrasion notch, (b) Author's (HM) hands after a day of belaying and climbing. (For interpretation of the references to color in this figure legend, the reader is referred to the web version of this article.)

particle limits [7], in the transition region between these limits [1], and of particle absorption over a broad range of κ [8]. Note that particles with $\kappa = 0$ are non-absorbing and completely white or shiny, possibly also reflective, with SSA = 1. However, particles with κ and its product with the size parameter x, i.e. κx, that are *both* larger than ~3, are *also* white or shiny with SSA ≈ 1, which explains the high reflectance of most *bulk* metals that behave similarly to large metal spheres with $\kappa > 3$ and $\kappa x > 3$ [9]. In addition to these extremes where SSA ≈ 1, four distinct regimes of absorption behavior have been identified for homogeneous, spherical particles in [8].

2. Everyday observations

Everyday observations of black particles are sometimes associated with black carbon [10] that, in the visible spectral ranges, has a complex refractive index of $m = n + \mathrm{i}\,\kappa = 1.95 + \mathrm{i}\,0.79$ [11] leading to a small SSA, and thus, a black appearance [10]. Indeed, black carbon (BC), in the form of nanotubes arranged in a forest-like array across a surface, is currently the blackest material ever produced, absorbing 99.995% of incident optical power across the visible spectrum [12]. In addition, particles from incomplete combustion of carbonaceous fuels [13,14] are often dominated by black carbon [10] with a blackish appearance and largely wavelength independent absorption, or by brown carbon [15,16] or minerals (e.g., iron oxides) [17,18] with a more brownish or reddish appearance and enhanced absorption at shorter visible and near-ultraviolet wavelengths [16].

However, the blackness of some objects need not be related to black carbon content but may be due to the presence of black metallic nanoparticles. Below, we will discuss everyday observations of bicycle drivetrains and rock-climbing ropes and argue that blackness in appearance occurs through use of these items causing the introduction of metallic nanoparticles via mechanical abrasion. In addition, we suspect that this effect also contributes to the rapid blackening of lubricating oil and grease, and of honing and cutting fluids. For example, metallic impurities in lubricating soft grease used in rail engines have been quantified with laser induced breakdown spectroscopy (LIBS) and shown to increase greatly in fully used grease when compared to fresh grease [19]. Furthermore, it was observed that the grease color changed from tan to black upon use [19].

2.1. Bicycle drivetrains

A typical bicycle drivetrain consists of a crankset that converts the reciprocating motion of a rider's legs into rotational motion of a chainring that drives a chain that in turn drives a cassette of rear sprockets (i.e., gears) connected to the rear wheel. A derailleur pulley moves the chain sprockets, thereby changing the gearing to allow the rider to vary the torque applied to the rear wheel. These components are made of metals (mostly steel and aluminum alloys, sometimes titanium) and are coated with lubricant (generally hydrocarbon-based oil) to reduce friction and abrasion. On a new bicycle, all metallic drivetrain components are clean, with a high-reflectance appearance. After use, however, black grime accumulates on these metal surfaces, even regular cleaning only briefly delays this process, see Fig. 1.

So, what makes this grime black? While oil can be pyrolyzed or charred at high temperature (≳300 °C) producing black carbon [20], such temperatures are not encountered by a bicycle drivetrain. Here we propose that abrasion, likely enhanced by mineral dust from the road that is entrained in the lubricant, produces metallic nanoparticles of black appearance. It is these particles, together with the lubricant, that form the black grime.

2.2. Rock climbing ropes

As another example, consider rock climbing. Climbers are often lowered to the ground by a belayer, with the loaded rope running through a metal carabiner, Fig. 2a, or ring fastened to the rock-wall at the top of the climb. Often, this gives the rope and the belayer's hands a greyish appearance, see Fig. 2b. Analogous to the lubricant with the bicycle example, the gray appearance of this grime cannot be explained by heat-based degradation of the rope material.

In light of Fig. 2, we again ask where this greyish appearance comes from and argue that black metallic nanoparticles are responsible for this appearance by partially covering the whitish hand and thereby leading to a greyish appearance. While a clean rope causes little abrasion of the metal carabiner, during outdoor climbing, ropes frequently contact the ground and mineral dust becomes imbedded into the rope's synthetic fiber weave. This is especially true for climbing on volcanic tuff (e.g., Owens River Gorge, California, USA), where the soil contains large amounts of fine-grained volcanic ash or tuff [21] that readily gets imbedded into the rope and makes it act like sandpaper. Such dust leads to the abrasion of significant quantities of metal from carabiners or rings used for frequent lowering. A notch in a carabiner due to this process is indicated by a red arrow at the inside bottom of the carabiner in Fig. 2a. Small metal particles resulting from this abrasion process become imbedded in the rope, and subsequently, some transfer to the belayer's hands, giving them the greyish appearance seen in Fig. 2b.

3. Theory

To investigate our hypothesis that black metallic nanoparticles can contribute to the black materials in Figs. 1 and 2, we use Mie theory to

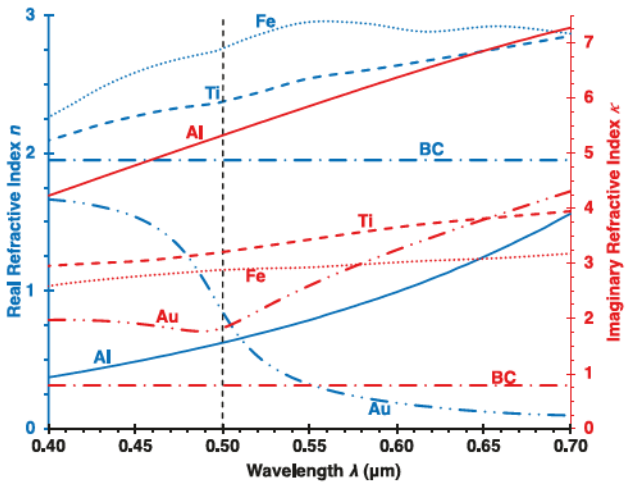

Fig. 3. Refractive index spectra for aluminum (Al), iron (Fe), titanium (Ti), gold (Au), and black carbon (BC). The left vertical-axis and blue lines correspond to the real part of the index, $n = Re\{m(\lambda)\}$ and the right vertical-axis and red lines correspond to the imaginary part, $\kappa = Im\{m(\lambda)\}$. The refractive index data originate from [11,23,24]. The vertical dashed line indicates the wavelength of $\lambda = 0.5$ μm used for calculations below.. (For interpretation of the references to color in this figure legend, the reader is referred to the web version of this article.)

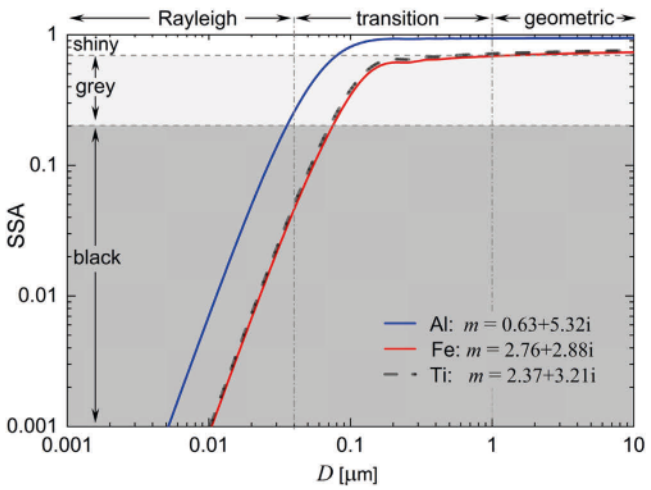

Fig. 4. Single scattering albedo (SSA) as function of particle diameter D, calculated with Mie theory for Al, Fe, and Ti at a wavelength of $\lambda = 0.5$ μm and plotted on a log–log scale. Horizontal dotted lines approximately separate regions in which the particles appear white ($SSA > 0.7$), gray ($0.2 < SSA < 0.7$), and black ($SSA < 0.2$). Vertical dashed lines approximately separate the Rayleigh ($D < 0.04$ μm), transition ($0.04 < D < 1$ μm), and geometric optics regime ($D > 1$ μm). (For interpretation of the references to color in this figure legend, the reader is referred to the web version of this article.)

calculate the SSA for homogeneous, spherical particles representative of metallic nanoparticles from their complex refractive index m and their size parameter x. For the metals of interest here, m varies sufficiently with wavelength λ that the scale invariance rule [22] cannot be applied, which necessitates replacing the size parameter x with the particle diameter D and wavelength λ. As we are interested in the visual appearance, we choose the mid-visible wavelength $\lambda = 0.5$ μm for our initial calculations.

3.1. Refractive indices for some metals

Relevant metals for the abraded nanoparticles discussed in Section 2 include aluminum (Al), iron (Fe), and titanium (Ti). However, as we will see in Section 4, other metals and non-metals are also present. Complex refractive index spectra $m(\lambda)$ for Al are given by McPeak et al. [23] and for Fe and Ti by Johnson and Christy [24]. We show these spectra for the visible spectral region ($\lambda = 0.4$–0.7 μm) in Fig. 3, demonstrating that m spectra for Fe and Ti are similar, yet quite different from the spectrum of m for Al. For our SSA calculations, we extract complex refractive indices in the mid-visible ($\lambda = 0.5$ μm) from the published data to find $m = 0.626+5.32i$ for Al, $m = 2.76+2.88i$ for Fe, and $m = 2.37+3.21i$ for Ti. In addition, refractive index spectra for gold (Au), given by McPeak et al. [23] and for black carbon [10], given by Bond and Bergstrom [11], are also included in Fig. 3. These will be used in Section 3.3 to investigate the coloration of metallic nanoparticles, as gold nanoparticles are known for their deep red color [5] and black carbon nanoparticles for their deep black appearance [25].

3.2. Single scattering albedo (SSA) as function of particle diameter

Using Mie theory with the complex refractive indices specified above, Fig. 4 shows that Al is the most reflective of the metals considered, having the largest value for the SSA. For Fe and Ti, the SSA is significantly smaller than that of Al for all particle diameters and differences in the SSA among these metals are small, i.e., <10%. Small particles, which are defined here as $D < 0.04$ μm or $x < 0.25$, reside in the Rayleigh regime where the SSA is proportional to their volume, or D^3. Large particles, defined by $D > 1$ μm or $x > 6.3$, reside in the geometric optics regime where the SSA is independent of D in agreement with everyday experience [7,8]. Between these limits lies the transition regime, where the SSA evolves from its D^3 dependence to being independent of D and where the rigorous Mie-theory description can be approximated by anomalous diffraction theory [1]. Note, however, that the boundaries between these regimes, as shown in Fig. 4, are only rough estimates [1,7].

Consider Fig. 4 again where the SSA is plotted as a function of particle diameter D. Large particles ($D > 1$ μm) show an SSA > 0.7, which indicates a white appearance. However, this is no longer true for small particles in the Rayleigh regime ($D < 0.04$ μm) where the SSA < 0.2 indicating a black appearance. In other words, for aluminum, iron and titanium particles to appear black, their diameter must to be less than 35 nm for aluminum and less than 75 nm for iron and titanium particles.

3.3. Particle color in the Rayleigh regime

Above, we have shown that small metal particles including those made of Al, Fe, and Ti are very dark or black at small diameters (i.e., $D < 0.04$ μm). However, these calculations were done for only one wavelength (i.e., $\lambda = 0.5$ μm) and a related question pertains to the color of these particles. This is connected to the long known fact that metallic gold (Au) nanoparticles have a deep red color [5], raising the question if Al, Fe, and Ti nanoparticles may also be strongly colored. Here, we do not address this question with color theory that involves complications of illumination and human color perception [26,27] but through comparison with the optical properties of black carbon and gold nanoparticles that are known for their deep black and deep red color, respectively.

For this comparison, we use Rayleigh theory, appropriate for calculation of nanoparticle SSA spectra from complex refractive index spectra. Rayleigh theory uses the quasistatic approximation, with the Lorentz–Lorenz (LL) factor $LL(m)$ [28,29] given by

$$LL(m) = \frac{m^2 - 1}{m^2 + 2}, \tag{2a}$$

with $F(m)$ and $E(m)$ conventionally used to denote the absolute square and the imaginary part of $LL(m)$, respectively [30] as

$$F(m) = |LL(m)|^2 \quad \text{and} \tag{2b}$$

$$E(m) = \mathrm{Im}\{LL(m)\}, \tag{2c}$$

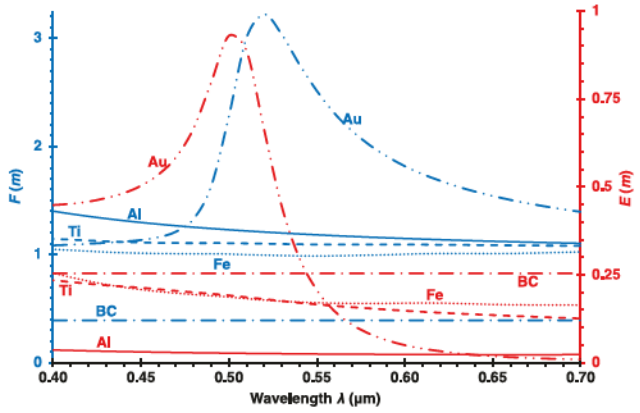

Fig. 5. LL factors $F(m)$ (blue lines, proportional to scattering cross section) and $E(m)$ (red lines, proportional to absorption cross section) spectra for aluminum (Al), iron (Fe), titanium (Ti), gold (Au), and black carbon (BC). Note that only the Au spectra have a significant wavelength dependence, the spectra for the other three metals are fairly flat as function of wavelength λ, similar to the totally flat black carbon spectra.. (For interpretation of the references to color in this figure legend, the reader is referred to the web version of this article.)

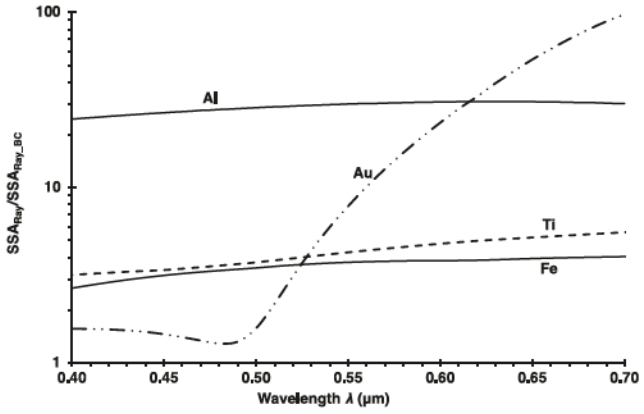

Fig. 6. Black carbon-normalized SSA spectra on a logarithmic scale for aluminum (Al), iron (Fe), titanium (Ti), and gold (Au). Note that only the Au spectrum has a significant wavelength dependence, the SSA of the other three metal nanoparticles as function of wavelength λ behaves similarly to that of black carbon that has a deeply black appearance, resulting in fairly flat lines.

where for the metals of interest, the complex refractive index m is a function of wavelength λ, as can be seen in Fig. 3.

In the Rayleigh regime ($D << \lambda$), Rayleigh particle scattering and absorption cross-sections C_{sca_Ray} and C_{abs_Ray} are proportional to $F(m)$ and $E(m)$, respectively, and can be written as

$$C_{sca\_Ray}(V,\lambda,m) = 24\pi^3 \frac{V^2}{\lambda^4} F(m) \quad \text{and} \tag{3a}$$

$$C_{abs\_Ray}(V,\lambda,m) = 6\pi \frac{V}{\lambda} E(m), \tag{3b}$$

where $V = \pi/6D^3$ is the particle volume. Fig. 5 shows the LL factors $F(m)$ and $E(m)$, proportional to scattering and absorption cross-sections, respectively, as function of wavelength for the visible spectral region between 0. 4 and 0.7 μm. For calculation of $F_{BC}(m)$ and $E_{BC}(m)$, we used the wavelength-independent black carbon refractive index $m_{BC} = 1.95 + i\ 0.79$ recommended by Bond and Bergstrom [11] for the visible range; this yields $F_{BC} = 0.392$ and $E_{BC}(m) = 0.255$. Note however that Liu et al. [31] recently have given a critical discussion of the black carbon complex refractive index and concluded that its real part should be somewhat lower (i.e., n and κ should be in the ranges of $1.5 < n < 1.86$ and $0.68 < \kappa < 1$).

Also note that the LL factors $F(m)$ and $E(m)$ are wavelength independent for black carbon (no dispersion) in the visible and show far less wavelength dependence for Al (i.e., 1.27, 1.57), Fe (i.e., 1.06, 1.58), and Ti (i.e., 1.07, 1.88) than for Au (i.e., 2.96, 99.9), where the first number in the brackets is the ratio between the maximum and minimum of $F(m)$ and the second number in the brackets is the ratio between the maximum and minimum $E(m)$ in the visible spectrum.

For absorbing particles in the Rayleigh regime, the SSA can be approximated as [7]

$$SSA_{Ray}(V,\lambda,m) = 4\pi^2 \frac{V}{\lambda^3} \frac{F(m)}{E(m)}. \tag{4}$$

This approximation is valid in the "black" ($SSA < 0.2$) region of Fig. 4, where SSA is proportional to the particle volume or D^3. For a comparison of SSA_{Ray} with that of black carbon that has a deeply black appearance, we further normalize SSA_{Ray} to that of black carbon (i.e., SSA_{Ray_BC}) to yield SSA_{Ray_norm} as

$$SSA_{Ray\_norm}(m) = \frac{SSA_{Ray}(V,\lambda,m)}{SSA_{Ray\_BC}(V,\lambda,m)} = \frac{E_{BC}(m)}{F_{BC}(m)} \frac{F(m)}{E(m)}, \tag{5}$$

where this normalization also removes the explicit dependence of SSA_{Ray} on particle volume V and wavelength λ.

This black carbon normalized SSA_{Ray_norm} is shown in Fig. 6 demonstrating a strong wavelength dependence for Au with much higher (factor of 75) SSA_{Ray_norm} in the red spectral region causing the typical red color of Au particles in the Rayleigh regime. For Al, Fe, and Ti, the wavelength dependence is much weaker with ratios between the maximum and minimum SSA_{Ray_norm} being 1.26, 1.54, and 1.77, respectively. This more than 40-times weaker wavelength dependence indicates a colorless appearance of Al, Fe, and Ti particles in the Rayleigh regime, similar to that of black carbon, when compared to the strongly colored Au particles.

4. Electron microscopy analysis

To investigate if the hypothesized metal nanoparticles are indeed present in the bicycle drivetrain and climbing rope grime, we performed transmission electron microscopy with energy-dispersive X-ray spectroscopy (TEM-EDX) analysis of grime samples. This analysis allowed us to determine particle size and elemental composition as needed to substantiate our claim of the presence of metallic nanoparticles. Three samples were considered: (1) a swab of grime from a bicycle chain (Shimano Model CN-HG700-11) that had been used for about one year (~2800 km) in a drivetrain consisting of this chain, and otherwise 4 year old (~15000 km) components including a Shimano FC-6800 crankset with 46X34T chainrings, a Shimano CS-6800 Ultegra 11-speed cassette, a Shimano FD-6800 Ultegra front double derailleur, and a Shimano RD-6800 Ultegra GS 11-speed rear derailleur), (2) a swab of grime from a pulley of the rear derailleur of the same drivetrain, and (3) a cutting of the outer sheath of a well-used (~10 years old) rock-climbing rope (Edelweiss Ally, 10.3 mm x 70 m). For brevity, we denote these samples as "chain", "pulley", and "rope", respectively. Each sample was placed in ethanol to dissolve the grime, which was sonicated for 15 min to help disperse any particles that may have remained. A drop of the ethanol-based suspension was then applied to a 200 mesh copper TEM grid with a carbon substrate. Lastly, the grids were placed under an incandescent heat-lamp to evaporate the ethanol, placing suspended particles on the TEM grid.

The TEM-EDX analysis was performed on a 200 kV FEI Tecnai F20 XT system operated at 120 kV providing a magnification of 235000× with an image resolution of 0.2 nm. Elemental analysis was provided by a Si(Li) EDAX detector coupled to the TEM. With this detector, integrated EDX spectra were produced from within regions of interest (ROI) in the TEM image, which quantifies the relative abundance of elements contained in the sample within the ROI. In addition, the elemental content can be mapped onto the TEM image within the ROI for specific elements revealing the spatial distribution of elements.

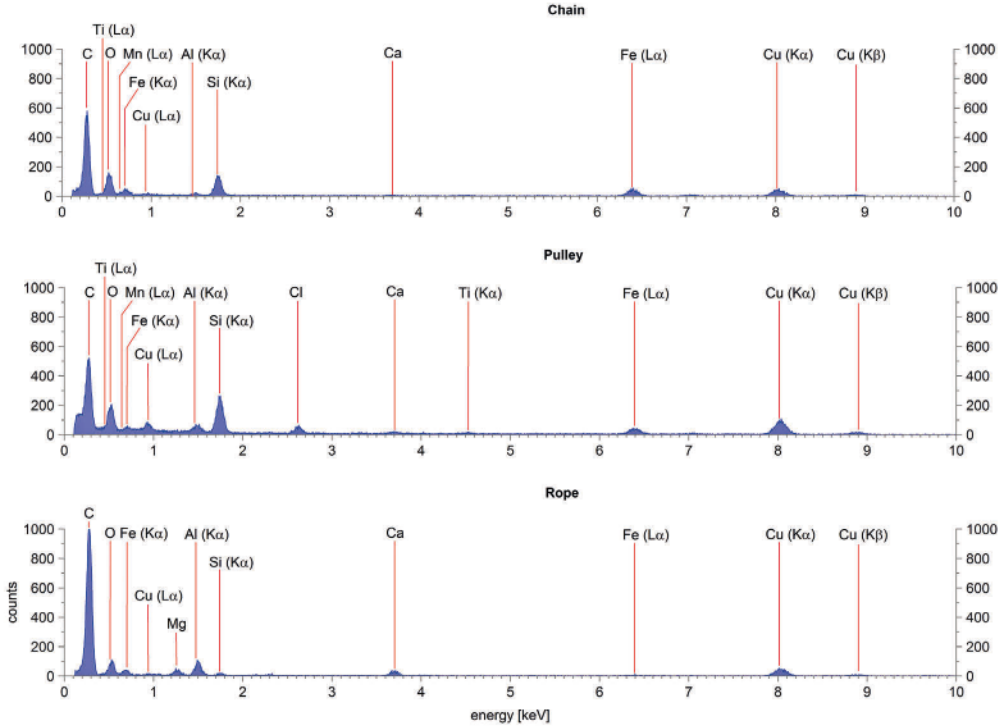

Fig. 7. Transmission electron microscopy energy-dispersive X-ray spectroscopy (TEM-EDX) analysis of grime samples. Two samples were taken from a used bicycle drivetrain: one from the chain, labeled "chain", and another from the derailleur pulley, labeled "pulley". The third sample was taken from a well-used climbing rope, labeled "rope". The EDX spectra are shown in blue for each sample with peaks labeled by the corresponding elements with a red line connecting the peak and the label. (For interpretation of the references to color in this figure legend, the reader is referred to the web version of this article.)

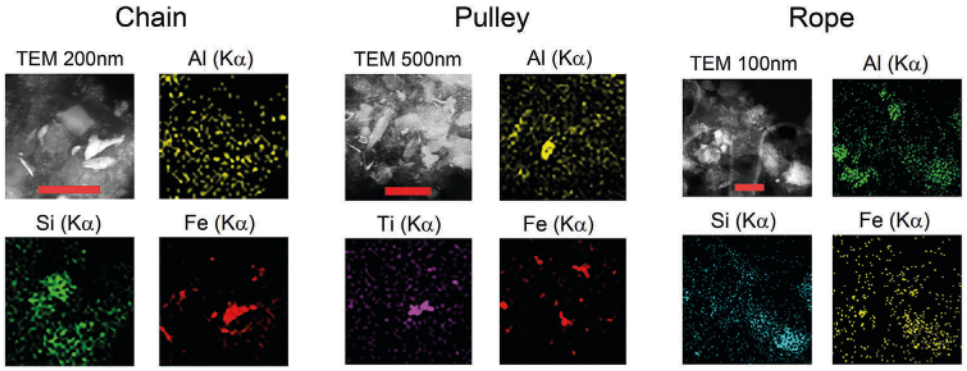

Fig. 8. Images showing the ROI in the TEM analysis of Fig. 7 and the spatial distribution of selected elements within this ROI. The images labeled "TEM xxx nm" denote the length of the (red) scale bar shown in the ROI image.. (For interpretation of the references to color in this figure legend, the reader is referred to the web version of this article.)

Fig. 7 shows the results of our TEM-EDX analysis. For each sample, the EDX spectra are shown for a given ROI in the TEM image of the sample. Each peak visible in the spectra is labeled by the corresponding electron transition of the element, e.g., Fe (K α), Fe (L α), etc. We see that C is the dominant element present, which could be due to the carbon substrate of the TEM grid or organics in the samples. Indeed, given the hydrocarbon nature of bicycle-chain lubricant and the carbon content of nylon rope, we expect to see large quantities of C in the samples. The presence of O could also be accounted for by this explanation. What is interesting here is that we see clear evidence for the presence of metals, particularly Al, Fe, and Cu. While the presence of Cu could be due to the TEM grid, there appear to be no obvious sources for Al and Fe other than that they come from abrasion of the metal surfaces of the bicycle drive train or of the Al or steel carabiner in the case of the rope.

Further evidence for this conclusion is provided in Fig. 8 from four images shown for each sample. First, consider those for the chain sample. The image labeled "TEM 200 nm" shows the TEM ROI where the red scale bar in the image has a length of 200 nm. In the other samples, the scale bar is similarly indicated by the image label. This image reveals the general morphology of the sample at the nanoscale, where for all samples, nanoparticles are visible. The accompanying images give the spatial distribution of a single element, indicated by the image label throughout the same ROI. Importantly, these images reveal that the elements considered *were not* distributed in the ROI in a diffuse manner, but rather were concentrated in regions consistent with specific nanoparticles visible in the TEM images. Moreover, consider the Fe element map for the chain sample and compare it to the other three images. Here, one sees a distinct region of red in the Fe map that is consistent with an irregular shaped nanoparticle in the TEM image. This same region shows little signal in the other element maps, Al and Si, suggesting that this particle was mostly Fe in composition, or perhaps, a compound with another element for which a map was not collected, i.e., O or C.

5. Future work and implications

While the blackening of bicycle drivetrains and rock-climbing ropes is a common fact, well known to bicyclists, bicycle mechanics, and rock climbers, we are not aware of any previous, reasonable explanation of these optical phenomena. Here, we give such an explanation based on basic electromagnetic theory and on observations of metallic nanoparticles on bicycle drivetrains and ropes. However, to further substantiate our observations, improved sampling and analysis procedures need to be developed to strengthen the causal relationship between the production of metallic nanoparticles through abrasion and the black appearance of grime. This work also needs to be expanded to other blackening processes, potentially caused by abrasion-produced metallic nanoparticles, such as the rapid blackening of lubricating oil and grease, and of honing and cutting fluids.

If indeed present, the implication of such metallic nanoparticles on human health are also of great interest and should be investigated. For example, metallic nanoparticles generated during rock climbing may be toxic and may enter the human body through dermal absorption [32]. Such particles are also likely to be produced and entrained into the ambient air when the climbing rope runs through the belay device, which is in close enough proximity to the belayer to be inhaled, or in machine shops where grinding, honing, milling, and lathing are common activities. While this process has not been studied, such metallic aerosols are likely to be inhaled and are potentially toxic [33]. Therefore, further study of metallic nanoparticle production through abrasion, their optical properties, their transport in the environment leading to human exposure, and their health impacts is urgently needed.

Funding

National Science Foundation, United States (1544425, 1665456, 1649783); NASA ROSES, United States (NNX15AI48G); Air Force Office of Scientific Research, United States (FA9550-19-1-0078).

Declaration of competing interest

The authors declare that they have no known competing financial interests or personal relationships that could have appeared to influence the work reported in this paper.

Acknowledgments

We thank Dr. Arjun Nepal of Kansas State University for his valuable suggestions during TEM data collection and Dr. Prem S. Thapa Chetri of the University of Kansas Microscopy and Analytical Imaging Laboratory for assistance with the TEM-EDX analysis.

References

[1] H. Moosmüller, C.M. Sorensen, Single scattering albedo of homogeneous, spherical particles in the transition regime, J. Quant. Spectrosc. Radiat. Transfer 219 (2018) 333–338.
[2] P. Chýlek, J. Wong, Effect of absorbing aerosol on global radiation budget, Geophys. Res. Lett. 22 (1995) 929–931.
[3] T. Hassan, H. Moosmüller, C.E. Chung, Coefficients of an analytical aerosol forcing equation determined with a Monte-Carlo radiation model, J. Quant. Spectrosc. Radiat. Transfer 164 (2015) 129–136.
[4] H. Moosmüller, J.A. Ogren, Parameterization of the aerosol upscatter fraction as function of the backscatter fraction and their relationships to the asymmetry parameter for radiative transfer calculations, Atmosphere 8 (2017) http://dx.doi.org/10.3390/atmos8080133.
[5] G. Mie, Beiträge zur Optik trüber Medien, speziell kolloidaler Metallösungen, Ann. Physik 330 (1908) 377–445.
[6] C.F. Bohren, D.R. Huffman, Absorption and Scattering of Light By Small Particles, Wiley, 1998.
[7] H. Moosmüller, C.M. Sorensen, Small and large particle limits of single scattering albedo for homogeneous, spherical particles, J. Quant. Spectrosc. Radiat. Transfer 204 (2018) 250–255.
[8] C.M. Sorensen, J.B. Maughan, H. Moosmüller, Spherical particle absorption over a broad range of imaginary refractive index, J. Quant. Spectrosc. Radiat. Transfer 226 (2019) 81–86.
[9] W.W. Coblentz, The reflecting power of various metals, Bull. Bureau Stand. 7 (1910) 197–225.
[10] D.A. Lack, H. Moosmüller, G.R. McMeeking, R.K. Chakrabarty, D. Baumgardner, Characterizing elemental, equivalent black, and refractory black carbon aerosol particles: A review of techniques, their limitations and uncertainties, Anal. Bioanal. Chem. 406 (2014) 99–122.
[11] T. Bond, R. Bergstrom, Light absorption by carbonaceous particles: An investigative review, Aerosol. Sci. Tech. 40 (2006) 27–67.
[12] K. Cui, B.L. Wardle, Breakdown of native oxide enables multifunctional, free-form carbon nanotube-metal hierarchical architectures, ACS Appl. Mater. Interfaces 11 (2019) 35212–35220.
[13] H. Kim, J.Y. Kim, J.S. Kim, H.C. Jin, Physicochemical and optical properties of combustion-generated particles from a coal-fired power plant, automobiles, ship engines, and charcoal kilns, Fuel 161 (2015) 120–128.
[14] Y. Cheng, G. Engling, H. Moosmüller, W.P. Arnott, A.L.W. Chen, C.E. Wold, W.M. Hao, K.B. He, Light absorption by biomass burning source emissions, Atmos. Environ. 127 (2016) 347–354.
[15] R.K. Chakrabarty, M. Gyawali, R.L.N. Yatavelli, A. Pandey, A.C. Watts, J. Knue, L.W.A. Chen, R.R. Pattison, A. Tsibart, V. Samburova, H. Moosmüller, Brown carbon aerosols from burning of boreal peatlands: Microphysical properties, emission factors, and implications for direct radiative forcing, Atmos. Chem. Phys. 16 (2016) 3033–3040.
[16] H. Moosmüller, R.K. Chakrabarty, K.M. Ehlers, W.P. Arnott, Absorption Ångström coefficient, brown carbon, and aerosols: Basic concepts, bulk matter, and spherical particles, Atmos. Chem. Phys. 11 (2011) 1217–1225.
[17] J.P. Engelbrecht, H. Moosmüller, S. Pincock, P.K.M. Jayanty, T. Lersch, G.S. Casuccio, Technical note: Mineralogical, chemical, morphological, and optical interrelationships of mineral dust re-suspensions, Atmos. Chem. Phys. 16 (2016) 10809–10830.
[18] H. Moosmüller, J.P. Engelbrecht, M. Skiba, G. Frey, R.K. Chakrabarty, W.P. Arnott, Single scattering albedo of fine mineral dust aerosols controlled by iron concentration, J. Geophys. Res. 117 (2012) http://dx.doi.org/10.1029/2011JD016909.
[19] C. Dhiman, M.N. Reddy, K. Gulati, M.S. Khan, Detection of elemental composition of lubricating grease using laser induced breakdown spectroscopy, Lubricants 2 (2014) 223–236.
[20] J.A. Libra, K.S. Ro, C. Kammann, A. Funke, N.D. Berge, Y. Neubauer, M.-M. Titirici, C. Fühner, O. Bens, J. Kern, K.-H. Emmerich, Hydrothermal carbonization of biomass residuals: A comparative review of the chemistry, processes and applications of wet and dry pyrolysis, Biofuels 2 (2011) 71–106.
[21] S.K. Haldar, Introduction to Mineralogy and Petrology, Elsevier, 2014.
[22] M.I. Mishchenko, Scale invariance rule in electromagnetic scattering, J. Quant. Spectrosc. Radiat. Transfer 101 (2006) 411–415.
[23] K.M. McPeak, S.V. Jayanti, S.J.P. Kress, S. Meyer, S. Iotti, A. Rossinelli, D.J. Norris, Plasmonic films can easily be better: Rules and recipes, ACS Photonics 2 (2015) 326–333.
[24] P.B. Johnson, R.W. Christy, Optical constants of transition metals: Ti, V, Cr, Mn, Fe, Co, Ni, and Pd, Phys. Rev. B 9 (1974) 5056–5070.
[25] H. Moosmüller, R.K. Chakrabarty, W.P. Arnott, Aerosol light absorption and its measurement: A review, J. Quant. Spectrosc. Radiat. Transfer 110 (2009) 844–878.
[26] G. Wyszecki, W.S. Stiles, Color Science: Concepts and Methods, Quantitative Data and Formulae, Wiley, 1982.
[27] R. Hirschler, P. Csillag, P. Manyé, M. Neder, How much colour science is not too much?, Color Res. Appl. 43 (2018) 977–992.
[28] H.A. Lorentz, Ueber die Beziehung zwischen der Fortpflanzungsgeschwindigkeit des Lichtes und der Körperdichte, Ann. Physik 245 (1880) 641–665.
[29] L. Lorenz, Ueber die Refractionsconstante, Ann. Physik 247 (1880) 70–103.
[30] C.M. Sorensen, Light scattering by fractal aggregates: A review, Aerosol Sci. Tech. 35 (2001) 648–687.
[31] F. Liu, J. Yon, A. Fuentes, P. Lobo, G.J. Smallwood, J.C. Corbin, Review of recent literature on the light absorption properties of black carbon: Refractive index, mass absorption cross section, and absorption function, Aerosol Sci. Tech. 54 (2020) 33–51.
[32] M. Crosera, M. Bovenzi, G. Maina, G. Adami, C. Zanette, C. Florio, F. Filon Larese, Nanoparticle dermal absorption and toxicity: A review of the literature, Int. Arch. Occup. Environ. Health 82 (2009) 1043–1055.
[33] S. Park, Y.K. Lee, M. Jung, K.H. Kim, N. Chung, E.-K. Ahn, Y. Lim, K.-H. Lee, Cellular toxicity of various inhalable metal nanoparticles on human alveolar epithelial cells, Inhal. Toxicol. 19 (2007) 59–65.